Technical Sciences, 2025, 28, 291–290

UNIWERSYTET WARMIŃSKO-MAZURSKI W OLSZTYNIE

Yearbook peer-reviewed scientific journal
ISSN 1505-4675
e-ISSN 2083-4527
TECHNICAL SCIENCES
Homepage: https://czasopisma.uwm.edu.pl/index.php/ts/

DOI: https://doi.org/10.31648/ts.12092

THE COMPARISON OF IONOSPHERIC TROUGH SIGNATURES DERIVED FROM GNSS DATA – A GEOMAGNETIC STORM CASE STUDY

Rafal Sieradzki

ORCID: 0000-0001-9496-9514
Department of Geodesy
Faculty of Geoengineering
University of Warmia and Mazury in Olsztyn

Received 13 December 2025, accepted 15 December 2025, available online

K e y w o r d s: GNSS, ionospheric trough, global ionospheric maps, geomagnetic storm.

A b s t r a c t

Nowadays, observations from the Global Navigation Satellite System (GNSS) are one of the most valuable datasets used for ionosphere remote sensing. One of the fields of such studies is to detect and describe the different-scale ionospheric effects, including the main ionospheric trough. This phenomenon is recognised as a large-scale depletion in plasma density with sharp gradients at the edges, observed at the boundary between the high- and middle-latitude ionosphere. Due to the connection between the trough and auroral oval, it exhibits a high dependence on the geomagnetic activity. This work presents a cross-evaluation of ionospheric trough detection using various GNSS-based methods. The assessment utilises multi-station geometry-free (GF) linear combination (LC) GNSS data, converted to vertical directions, and global ionospheric maps. In the former case, data from several dozen stations located in the Northern Hemisphere are used to provide a spatial view of the analysed ionospheric phenomenon. The study focuses on the patterns of trough during high geomagnetic activity that occurred in March 2012. The results confirm that the network-derived GF LC GNSS time series, scaled to a vertical ionospheric path, can be successfully used for ionospheric trough monitoring. Such datasets provide complex signatures of trough during two selected cases corresponding to different phases of the storm. In contrast, the results derived from the global ionospheric maps suffer from generalisation, the level of which depends

Correspondence: Rafal Sieradzki, University of Warmia and Mazury in Olsztyn, Oczapowskiego 1 St., 10-719 Olsztyn, e-mail: rafal.sieradzki@uwm.edu.pl

on the generating algorithm. The comparison of such products provided by UPC and ESA reveals the outperformance of the former, characterised by RMS values at the level 1.7-1.8 TECu. In contrast, the patterns of ionospheric trough in the ESA product are significantly deteriorated, even to 4.4 TECu RMS.

Introduction

The Global Navigation Satellite System (GNSS) is a powerful technique used in a broad spectrum of earth sciences. The crucial applications include navigation, satellite positioning, and atmospheric investigations, involving both the troposphere and the ionosphere (HERNÁNDEZ-PAJARES et al. 2011, BRANZANTI et al. 2013, PAZIEWSKI 2015, BANVILLE et al. 2017). Among those mentioned above, particularly interesting is the coupling between GNSS measurements and the ionised part of the atmosphere. On the one hand, the free electrons deteriorate GNSS signals. Still, on the other hand, the application of multi-frequency signals allows us to utilise the geometry-free (GF) GNSS data (also called L_4/P_4 linear combinations (LC) for phase and code measurements, respectively) as a sensitive sensor of the ionospheric impact. Taking into account the latter advantage, GNSS-based ionospheric investigations include two main directions: regional/global vertical total electron content (VTEC) mapping and forecasting (KOMJATHY et al. 2005, JAKOWSKI et al. 2011, LI et al. 2015, REN et al. 2016) as well as the detection of plasma irregularities (WAUTELET, WARNANT 2014, SIERADZKI 2015, TSAGOURI, BELEHAKI 2015, NING, TANG 2018). The investigations in the former group typically estimate the average state of the ionosphere, taking into account hardware biases. At the same time, the latter leverages the temporal variation of raw, geometry-free series.

The shape and complexity of the ionosphere depend strongly on various physicochemical processes and interactions with other atmospheric layers, as well as space weather conditions. Consequently, the most complex structure is observed for polar and auroral areas (BOWLINE et al. 1996, KULLEN et al. 2002, PRIKRYL et al. 2015, SIERADZKI, PAZIEWSKI 2019), where the lines of the geomagnetic field intersect the ionosphere, creating a window for the transfer of solar energy. The connection between the magnetosphere and the ionosphere drives the high-latitude convection pattern and is responsible for generating large-scale phenomena, such as polar patches, as well as smaller-scale irregularities that form the auroral oval. It also supports the generation of depletion in electron density, known as the main or middle-latitude ionospheric trough (AA et al. 2020, PEREVALOVA et al. 2020, LUBYK et al. 2022). This phenomenon occurs directly below the auroral oval and consists of three main parts: the poleward and equatorward walls, separated by the depression in plasma amount. The trough corresponds to the variation in the nighttime F-region of the ionosphere that typically occurs between 50° and 70° of geomagnetic latitude. Still, its actual position depends on many factors, including season, geomagnetic/solar activity, and magnetic local time (WERNER, PRÖLSS 1997, HE et al. 2011, ISHIDA et al. 2014). The ionospheric trough is characterised by a long extension along the longitude, approximately within the range of 18:00 to 06:00 magnetic local time, and a relatively narrow width, reaching several degrees in latitude. The main processes believed

to be responsible for the generation of this phenomenon are: the stagnation mechanism, related to counteracting the corotation of the Earth and the polar convection (NILSSON et al. 2005, RODGER 2008), and amplified recombination rate following enhanced ion temperature (FOSTER, BURKE 2002, RODGER 2008).

The up-to-date analyses of the ionospheric trough utilised a broad spectrum of techniques, including, among others, in-situ measurements from low-Earth satellites, incoherent scatter radar, and GNSS (HORVATH, ESSEX 2003; LEE et al. 2011, ISHIDA et al. 2014, AA et al. 2020). Considering the latter technique, the investigations included both global/regional VTEC maps and analyses of geometry-free series variation (PRYSE et al. 2006, KRANKOWSKI et al. 2009, PEREVALOVA et al. 2020, ROYERSMITH et al. 2025). All these reports confirm the applicability of both GNSS-based algorithms. Consequently, there is no doubt that their potential will increase as the densification of ground-based networks of permanent stations progresses. Nevertheless, both approaches have advantages and disadvantages. Considering global VTEC maps, we obtain full spatial coverage for a specific time interval, but at the cost of generalisation driven by the function describing the ionosphere. On the contrary, geometry-free combination time series provide real slant TEC (STEC) information and thus, a true signature of the phenomenon, assuming the neglected impact of phase data noise. The weaknesses of the second methodology are gaps related to the distribution of stations and ambiguous absolute levels of STEC or VTEC values.

The existence of two widely adopted GNSS-based approaches motivates the cross-evaluation of the signatures of the ionospheric trough and a comparison of the corresponding results. For this purpose, an algorithm is adopted that converts the multi-station GF linear combination time series to a vertical ionosphere path, utilising global VTEC values for support. The case study analysis includes two cases corresponding to different states of the ionosphere.

The work is organised as follows. It starts with a description of geomagnetic activity during test days. The next section provides details of the methodology applied to derive the GF LC time series and their subsequent conversion to a vertical direction. Then, the real signatures observed in measurements, as well as their reflection in global VTEC maps, are demonstrated. Finally, the conclusions are drawn.

Geomagnetic conditions

To highlight the differences between the signatures of trough in the GF series and global VTEC maps, active geomagnetic conditions were selected. Thus, based on earlier results (SIERADZKI, PAZIEWSKI 2019), data collected in March 2012 were used, which constitute a highly disturbed period that extended practically for the entire month. To clarify the geomagnetic conditions, Figure 1 presents

the variations of the north-south component of the interplanetary magnetic field (IMF Bz) as well as two geomagnetic indices, AE (Auroral Electrojet) and SYM-H Symmetric-Horizontal), for a period from March 6 to 9, 2012. For this purpose, 1-minute values from the OMNI database (http://omniweb.gsfc.nasa.gov) were adopted, which is acknowledged.

As can be read from Figure 1 and SYM-H index values, two geomagnetic storms occurred on March 7 and 9. The first geomagnetic storm was initiated with the interplanetary shock observed in Advanced Composition Explorer spacecraft data at ~03:30 UTC on March 7, 2012 (TSURUTANI et al. 2014). Consequently, due to a negative IMF Bz, the main phase of the storm began, reaching its maximum of -98 nT at ~06:50 UTC. Simultaneously, the intensified auroral activity (AE index) was registered. As reported in (SIERADZKI, PAZIEWSKI 2019), the maximal extension of the auroral oval occurred at ~10:00 UTC. Over the next few hours, we observed the repeated reorientation of IMF Bz, which stabilised at a positive level around 22:00 UTC, terminating the activity in the auroral zone. Such conditions lasted until a positive impulse from the interplanetary shock, resulting in an abrupt increase of SYM-H to 54 nT (~11:06 UTC, March 8, 2012). As can be seen in Figure 1, the main phase of the second storm was, in this case, delayed and started after the north-to-south switch of the Bz component, which occurred at 2:20 UTC on March 9, 2012. Considering the second storm,

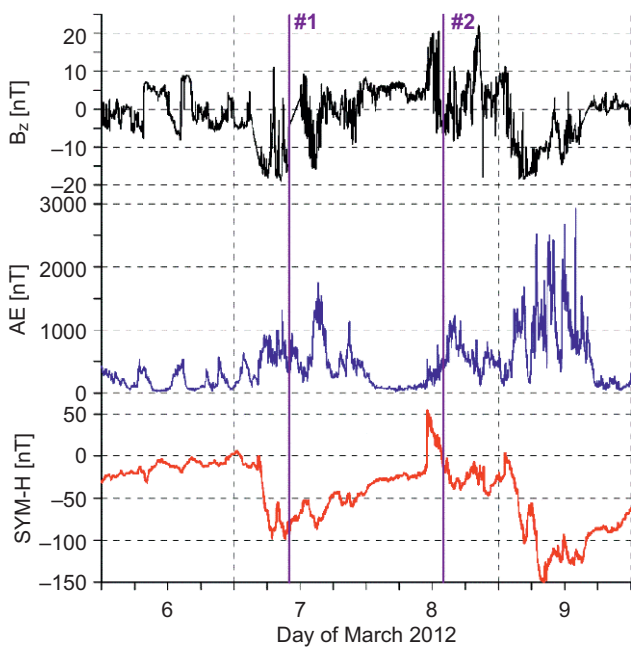

Fig. 1. Variations of the interplanetary magnetic field (IMF Bz) and geomagnetic parameters (AE, SYM-H) during March 6–9, 2012

the minimum of the SYM-H parameter equals -148 nT and was followed by very intense auroral activity up to 17:00 UTC.

Since the position and the poleward wall of the ionospheric trough are basically driven by the external boundary of the auroral oval, two different-condition cases, marked in Figure 1 as #1 and #2, are selected. The first of them, reported in (SIERADZKI, PAZIEWSKI 2019) using relative STEC values, corresponds to an extremely expanded oval during the main phase of the storm. The second, on the contrary, coincides with only slightly increased AE values following the interplanetary shock that initiated the storm on March 9, 2012. Thus, the still detectable poleward boundary of the trough is expected at higher latitudes. Furthermore, this event was preceded by a long period of quiet and a depleted ionosphere. The selection takes into account the distribution of permanent stations, allowing us to retrieve the signatures based on data from multiple stations.

Algorithm of ionospheric trough detection

The extraction of precise information on relative ionospheric variation is typically realised with the GF linear combination of phase GNSS data, also often denoted as L_4 (KRYPIAK-GREGORCZYK, WIELGOSZ 2018), and that notation is used in the equations. This combination takes the benefit from dual-frequency GNSS signals and can be written for the satellite k and receiver s according to the equation:

$$L_{4,s}^{k} = L_{1,s}^{k} - L_{2,s}^{k} = I_{4,s}^{k} + B_{4,s}^{k} \tag{1}$$

As can be seen from Equation 1, the outcome is basically a difference of phase data at both frequencies ($L_{1,s}^{k}$, $L_{2,s}^{k}$,) that eliminates all geometric and clock factors. Consequently, the equation can be rewritten as a sum of scaled, epoch-wise ionospheric delay ($I_{4,s}^{k}$) and term $B_{4,s}^{k}$), which couples the difference of ambiguity terms for both signals as well as the corresponding function of hardware delays. Since the latter factor can be assumed as a short-term constant, the entire variation in the GF series represents the impact of the ionosphere and thus, provides real information on the variability of this layer.

Examining the series, we should note that terms $B_{4,s}^{k}$ are specific for a particular arc and can be affected by cycle slips. To overcome these limitations, the following algorithm is adopted. Initially, the GF combination series is cleaned of cycle slips. Since these distortions are frequent under high-latitude storm-time conditions, they are repaired using code measurements with the following steps. At first, the cycle slips are identified using the between-epoch differences, with the threshold empirically set to 5 TECu/min. The setting of such a high

threshold is driven by a strongly variable ionosphere, which in extreme cases may approach this value. The feasibility of small cycle slips is further evaluated through a comparison of data from different stations. Then, for the subarcs with no distortions in phase measurements for at least 15-minute intervals, the series between epochs i and j are levelled with code data using the equation:

$$\tilde{L}^k_{4,s_{(i..j)}} = L^k_{4,s_{(i..j)}} - median(L^k_{4,s_{(i-j)}} + P^k_{4,s_{(i-j)}})_{subarc} =\approx -P^k_{4,s_{(i..j)}} \quad (2)$$

In cases of shorter periods with cycle slips, the algorithm leverages Equation 2 and allows us to replace $\tilde{L}^k_{4,s_{(i..j)}}$ with a five-epoch moving average of GF linear combination of pseudorange data ($-P^k_{4,s_{(i..j)}}$). Such processing slightly smooths the pattern of structures in the time domain, but it does not significantly distort the analysed signatures. This is particularly justified due to the frequent cycle slips occurring mostly above the poleward wall of the trough.

Since the clean dataset of phase GF LC($\tilde{L}^k_{4,s_{(i..j)}}$) represents the slant ionospheric information and depends on differential code biases, which vary between the satellites and receivers, we need to standardise them to a single level. Considering the purpose of the work, VTEC values from the global ionospheric map are utilised as a reference.

For this purpose, an epoch with no significant variation in the clean dataset is selected. For this data, which includes computed coordinates of the ionospheric piercing point, the VTEC value from the global map is interpolated and converted to a slant path using a single-layer model. Subsequently, the entire series of $\tilde{L}^k_{4,s_{(i..j)}}$ is shifted to the reference STEC value from the map ($\widetilde{STEC}^k_{4,s_{(i..j)}}$) and converted back to the vertical direction, providing the final $\widetilde{VTEC}^k_{4,s_{(i..j)}}$ values for a particular arc.

The functionality of the algorithm is presented in Figure 2, demonstrating the levelled time series in both the slant and vertical directions for the dataset from two American stations: GOBS and P023. The ($\widetilde{STEC}^k_{4,s_{(i..j)}}$) data are presented in blue, while the converted $\widetilde{VTEC}^k_{4,s_{(i..j)}}$ data are marked in black. The values are aligned to VTEC from hourly global ionospheric maps (GIM) generated and provided by Universitat Politècnica de Catalunya (UPC) at 12:00 UTC, in such a way as to fulfil two conditions: the possibly high elevation and a relatively quiet ionosphere. As one can observe, even in this initial view, the clear difference between the map and the actual signature is demonstrated. The global map basically reveals only the poleward wall of the trough with a peak around 11:00 UTC. In contrast to this, in the $\widetilde{VTEC}^k_{4,s_{(i..j)}}$ dataset, we see the entire signature of the analysed ionospheric phenomena, as well as the small-scale irregularities that occurred in the auroral oval area.

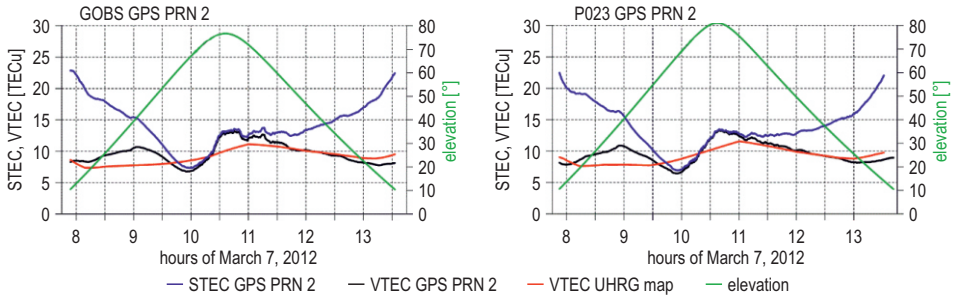

Fig. 2. GPS PRN 2 STEC and VTEC values from stations GOBS and P023 aligned to global ionosphere maps provided by UPC

The GNSS-based signatures of the ionospheric trough.

Based on the promising single-arc results, the focus is on comparing a multi-station $\widehat{VTEC}^{k}_{4,s_{(i..j)}}$ dataset with corresponding results from two global ionospheric products. Specifically, the hourly GIMs provided by the UPC and the European Space Agency (ESA) are used. These GIMs are generated using various algorithms, including the kriging interpolation method and the spherical harmonic expansion, respectively (Feltens 2007, Orús et al. 2005). Both of these analysis centres participate in generating a global International GNSS Service (IGS) product, recognised as the most precise source of information on the ionosphere. However, since the latter is a combined map, I decided to use the original UPC and ESA outcome.

To justify the selection of two global maps, derived using different algorithms, Figure 3 provides examples of these maps for the epoch of 10:00 UTC on March 7, 2012. The displayed products clearly demonstrate the expected discrepancies. Thus, the GIM of ESA, which takes advantage of spherical harmonic expansion, is much more generalised, while the UPC product provides more detailed information for specific areas. The most significant differences are observed in the equatorial region and southern middle latitudes, where an abnormal dayside TEC enhancement is noted below the auroral oval. The latter signature seems to be related to a storm-induced effect known as the tongue of ionisation. The occurrence of this large-scale phenomenon only in the case of UPC maps is likely associated with the different datasets used by particular centres, as well as the relatively low number of permanent stations in this area. Nevertheless, the apparent discrepancies also occur at high latitudes, including the night-side trough region.

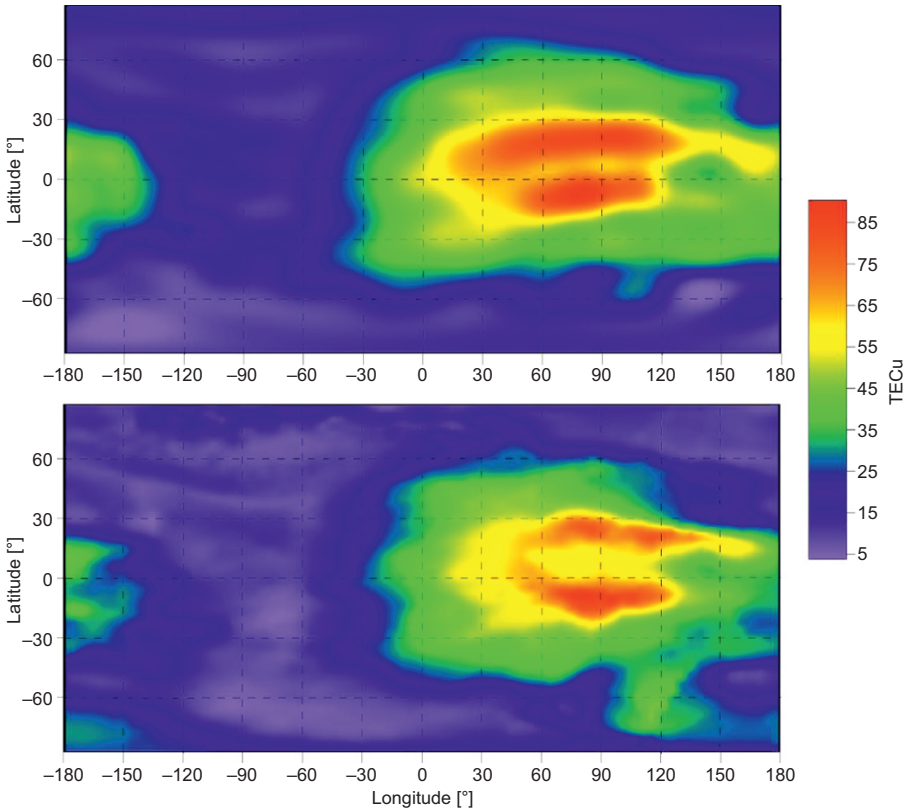

Fig. 3. The ionospheric maps provided by ESA (top panel) and UPC (bottom panel) for March 7, 2012, 10:00 UTC

The case on March 7, 2012

The first analysed case concerns the epoch marked in Figure 1 as #1, i.e., the signature of the ionospheric trough near the peak of the geomagnetic storm at 10:00 UTC on March 7, 2012. As AE values support it, we should expect an enormously expanded auroral oval and a moving ionospheric trough equatorwardly. For the presentation of an actual $\widetilde{VTEC}^{k}_{4,s_{(i..j)}}$ variation (referenced to the UPC map at epoch 12:00 UTC), the single-arc dataset from 16 stations, located in the west and central part of the United States and belonging to the Plate Boundary Observatory (PBO) mission (Figure 4) is used. The selected sites form a linear sub-network that allows clear visualisation of the ionospheric trough for different longitudes. The north-west to south-east distribution asymmetry is a consequence of the dependence of phenomenon boundaries on geomagnetic latitudes.

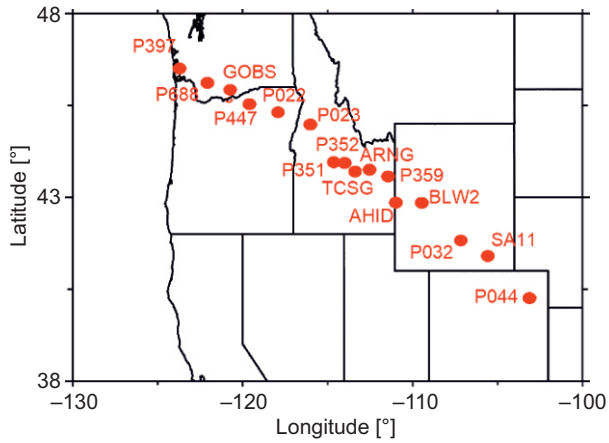

Fig. 4. The distribution of permanent stations used in the case on March 7, 2012

Figure 5 shows the comparison of the ionospheric trough signatures derived from the multi-station single-arc dataset of $\widehat{VTEC}^{k}_{4,s_{(i..j)}}$ and the global VTEC maps. In the former case, I interpolate the $\widehat{VTEC}^{k}_{4,s_{(i..j)}}$ surfaces using a triangulation method, assuming a linear change between samples, for the PRN 2 and PRN 4 GPS satellites. Since the VTEC GIM maps are provided in the geographical reference frame, this system is used for the visualisation.

Examining the outcome for case #1, we definitely see that signatures in $\widehat{VTEC}^{k}_{4,s_{(i..j)}}$ data reveal true gradients associated with the ionospheric trough. Accordingly, for both adopted GPS satellites, one can observe the expected pattern of this phenomenon, including pole- and equatorward boundaries separated by a depression in plasma amount. The latitudinal range of the trough, corresponding to a distance between the $\widehat{VTEC}^{k}_{4,s_{(i..j)}}$ peaks, equals to ~4°. The gradient at the poleward wall is significantly higher, and GPS PRN 2 exceeds even 5 TECu for a one-degree change in latitude. The narrow depression, located approximately at 44° of geographical latitude, is characterised by a reduction of electron content by 6 TECu as compared to the poleward peak.

In contrast to the detailed view in single-arc datasets, the outcome given by the GIMs is strongly spatially smoothed. As one might expect, the blurring of the ionospheric trough signature appears extreme in ESA maps. As a result, while we see a 2 TECu depletion in VTEC values approximately at 42° of latitude, there are no clear signatures of walls. Instead, we observe a gradual increase in VTEC values in both the pole and equator directions, respectively. It suggests that the spherical harmonics, used in ESA maps with settings for global VTEC representation, may not be suitable for trough

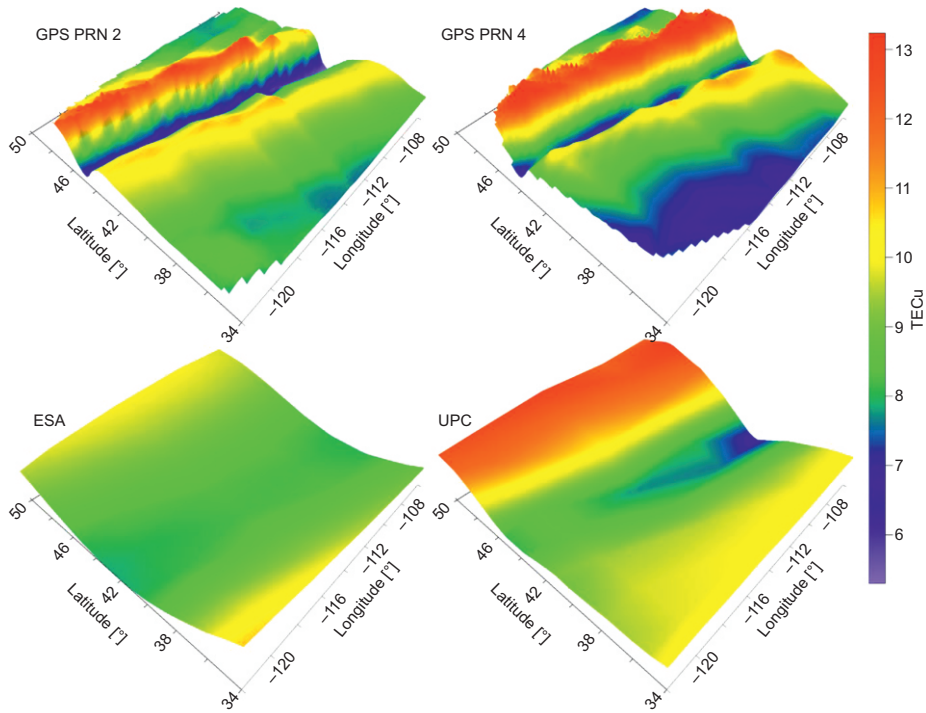

Fig. 5. The ionospheric trough signatures derived from the multi-station single-arc solutions (top panel) and global ionospheric maps (bottom panel) at 10:00 UTC on March 7, 2012

recognition. We get slightly better results for the UPC map. The latitudinal location of the trough is closer to a proper position (~43° of latitude), and we observe a much more pronounced signature of the poleward wall, resulting in a depletion of 4 TECu. Still, as a result of kriging interpolation, its peak is shifted toward high latitudes. Furthermore, similar to the ESA map, there is no clear signature of equatorward wall, but a slow increase in VTEC toward lower latitudes.

To depict the residuals and quantify the agreement between the true GF series and both GIMs, the longitudinal profiles for all solutions are provided in Figure 6. Since the signatures of trough reveal only a very weak dependence for different meridians, we select a longitude equal to -114° for this purpose. Examining the outcome for the ESA product, we observe the maximal residuals at both edges of the trough reaching up to 2.5 TECu and 3.8 TECu for equatorward and poleward walls, respectively. The profile for UPC GIM confirms the latitudinal smoothing of the trough signature. Thus, the maximal discrepancy between this product and the GF series occurs not

only at the true position of the analysed phenomena but also at the edges of the investigated area. Consequently, while the UPC map at least partly depicts the pattern of the ionosphere, the RMS values for both cases are very close, varying between 1.7 and 1.8 TECu.

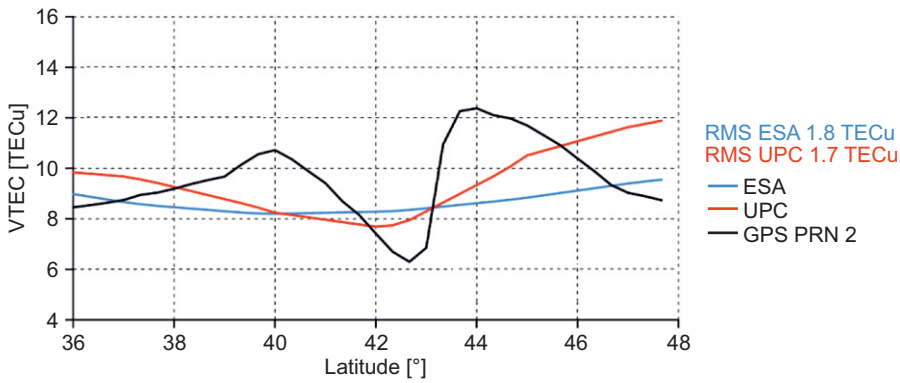

Fig. 6. The longitudinal profiles of VTEC for ESA and UPC GIMs as well as the corresponding values derived from a single-satellite solution using GPS PRN 2 data. The adopted longitude is equal to –114°

The case on March 8, 2012

The second analysed case, at 14:00 UTC on March 8, depicts the conditions immediately after a prolonged period of northward IMF Bz and a switch in orientation to south, marked in Figure 1 as #2. As a consequence, it connects the global depletion of VTEC, resulting from a negative recovery phase following the storm on March 7, and an initial phase of increased auroral activity. Thus, the ionospheric trough during test case #2 occurred at higher latitudes compared to the previously described one. Due to this reason, in the second experiment, GNSS data from PBO stations, which are primarily located in Alaska (Fig. 7), is used.

As in the case #1, the chosen sites create an almost linear sub-network that supports the detection of the ionospheric trough region. To ensure consistency, the outcome for test #2, as shown in Figure 8, includes the multi-station single-arc dataset of $\widetilde{VTEC}^{k}_{4,s_{(i..j)}}$ for two GPS satellites (PRNs 18 and 21), as well as the GIMs provided by ESA and UPC. In the former case, series are aligned to map at 16:00 UTC, March 8.

Analysing the actual signatures given in the top panel of Figure 8, we observe a completely different shape of the ionosphere for the trough region as compared to the case #1. While the auroral activity generates a notable poleward boundary

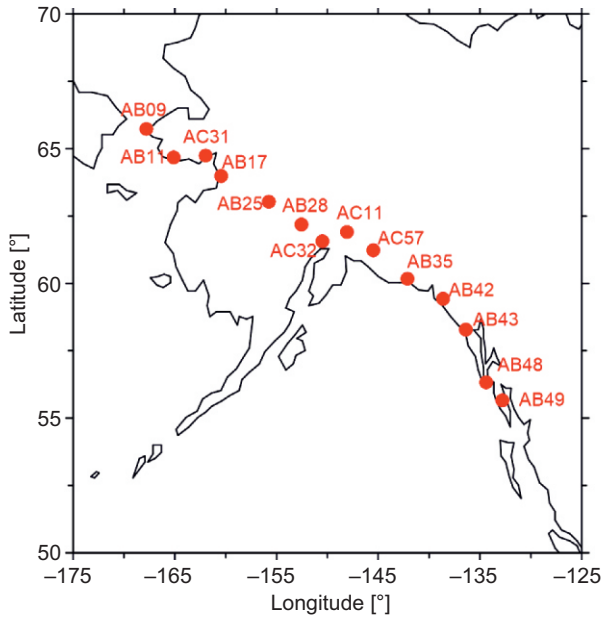

Fig. 7. The distribution of permanent stations used in the case on March 8, 2012

of the analysed phenomenon, there is no equatorward wall. Instead, one can observe an extended depletion, which according to global VTEC maps, reaches even 30° of latitude. As for the poleward boundary, the specific conditions during #2 implicated an extreme gradient that exceeds even 7 TECu per degree and even 10 TECu for the entire slope of the wall. As expected, the position of the upper trough edge is shifted to high latitudes, in this case, occurring at ~60° latitude. The comparison of results for both satellites also indicates a higher variability of $\widetilde{VTEC}^{k}_{4,s_{(i..j)}}$ values at the boundary between oval and trough for GPS PRN 21. This inconsistency seems to be related to a half-hour time shift between the two outcomes, and thus, different ionospheric conditions.

Examining the results for the ESA map, we see further confirmation of the product's low effectiveness in reflecting the conditions in the trough region over North America. Thus, in place of a sharp gradient, we observe a gradual decrease in VTEC values that extends practically across the entire 20° band, as shown in Figure 8. Consequently, despite revealing different VTEC levels for high and middle latitudes, we cannot use this map to describe the trough. On the contrary, we should remind that the distribution of stations used for generating the global map varies between longitudinal sectors, and thus, we cannot prejudge the low effectiveness of the ESA map for other regions. Examining the UPC outcome, we find it applicable to the ionospheric trough characterisation. While we observe

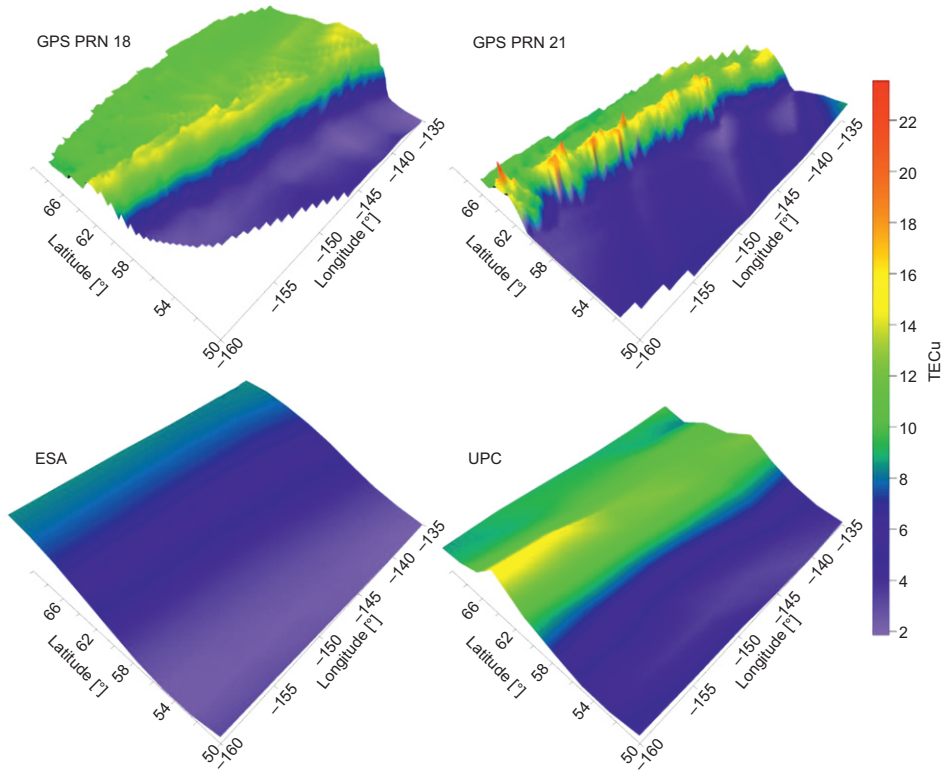

Fig. 8. The ionospheric trough signatures derived from the multi-station single-arc solutions (top panel) and global ionospheric maps (bottom panel) at 14:00 UTC on March 8, 2012

a smoothing in the latitude direction, the signature of the phenomenon is basically retained. Indeed, due to applied interpolation, the gradient of the poleward wall is significantly lower, i.e., up to 2 TECu per degree. On the other hand, both the position of the trough and the difference between the maximum of the poleward wall and the depletion equal to ~8 TECu, which should be classified as satisfying.

Finally, the profiles of VTEC for case #2 and longitude -147° are demonstrated in Figure 9. The comparison of outcomes from two GIMs with the GF series reveals a significantly better performance of the UPC product. As a result, while we see the effect of generalisation and residuals up to 4 TECu for the poleward edge, the pattern of UPC VTEC follows the true signature. In contrast, we observe an opposite situation for the ESA map, where the shape of VTEC is almost flat; thus, the differences between this GIM and single-satellite solution reach ~10 TECu. Consequently, the RMS values for #2 are equal to 1.8 and 4.4 TECu for the UPC and ESA products, respectively.

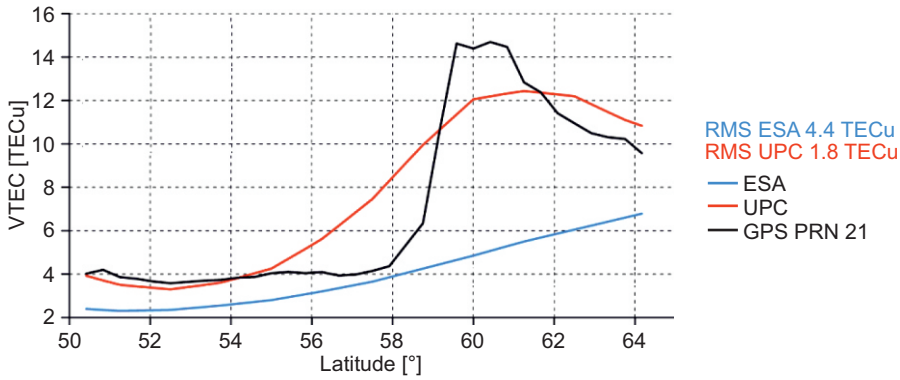

Fig. 9. The longitudinal profiles of VTEC for ESA and UPC GIMs as well as the corresponding values derived from a single-satellite solution using GPS PRN 21 data. The adopted longitude is equal to –147°

Conclusions

The objective of this work was to evaluate the effectiveness of the GNSS observations in detecting and characterising the ionospheric trough. Specifically, the true ionospheric signatures derived from single-arc geometry-free linear combination were compared with those obtained with global ionospheric maps, namely ESA and UPC maps, which are generated using different algorithms, i.e., spherical harmonic expansion and kriging interpolation, respectively. The investigations included two storm-time cases representing different ionospheric conditions over the American sector.

The detection of the ionospheric trough with geometry-free time series confirmed that their application allows the revelation of complex patterns of this phenomenon, even during different phases of a geomagnetic storm. Furthermore, the combined utilisation of multi-station data, levelled using global maps, enabled the spatial characterisation of the structure. Consequently, the extreme gradients, which reached several TECu per degree of latitude in the investigated examples, are observable.

On the contrary, the patterns of the trough in the global ionospheric maps were affected by different levels of generalisation, which varied strongly between the tested products. Considering the outcome provided by the ESA map, I find it unsuitable for describing the trough, at least in the American sector. The reason for this effect seems to be the adjustment of spherical harmonic settings for global ionosphere mapping. The much more detailed results were obtained with the UPC maps. Their supremacy appears to be driven by the use of kriging interpolation, which allows for better identification of local ionospheric phenomena.

Acknowledgments

This research was funded by the National Science Centre, Poland, Project No. 2023/48/Q/ST10/00059. For the purpose of Open Access, the author has applied a CC-BY public copyright licence to any Author Accepted Manuscript (AAM) version arising from this submission. The author is grateful for GNSS data and products provided by UNAVCO, IGS, ESA and UPC. I acknowledge the use of NASA/GSFC's Space Physics Data Facility's OMNIWeb service and OMNI data.

References

AA E., ZOU S., ERICKSON P.J., ZHANG S., LIU S. 2020. *Statistical Analysis of the Main Ionospheric Trough Using Swarm in Situ Measurements*. Journal of Geophysical Research: Space Physics, 125: e2019JA027583. https://doi.org/10.1029/2019JA027583

BANVILLE S., SIERADZKI R., HOQUE M., WEZKA K., HADAS T. 2017. *On the estimation of higher-order ionospheric effects in precise point positioning*. GPS Solutions, 21: 1817-1828. https://doi.org/10.1007/s10291-017-0655-0

BOWLINE M.D., SOJKA J.J., SCHUNK R.W. 1996. *Relationship of theoretical patch climatology to polar cap patch observations*. Radio Science, 31: 635-644. https://doi.org/10.1029/96RS00236

BRANZANTI M., COLOSIMO G., CRESPI M., MAZZONI A. 2013. *GPS Near-Real-Time Coseismic Displacements for the Great Tohoku-oki Earthquake*. IEEE Geosci. Remote Sensing Letters, 10: 372-376. https://doi.org/10.1109/LGRS.2012.2207704

FELTENS J. 2007. *Development of a new three-dimensional mathematical ionosphere model at European Space Agency/European Space Operations Centre*. Space Weather, 5: 2006SW000294. https://doi.org/10.1029/2006SW000294

FOSTER J.C., BURKE W.J. 2002. *SAPS: A new categorization for sub-auroral electric fields*. Eos, Transactions American Geophysical Union, 83: 393-394. https://doi.org/10.1029/2002EO000289

HE M., LIU L., WAN W., ZHAO B. 2011. *A study on the nighttime midlatitude ionospheric trough*. Journal of Geophysical Research: Space Physics, 116. https://doi.org/10.1029/2010JA016252

HERNÁNDEZ-PAJARES M., JUAN J.M., SANZ J., ARAGÓN-ÀNGEL À., GARCÍA-RIGO A., SALAZAR D., ESCUDERO M. 2011. *The ionosphere: effects, GPS modeling and the benefits for space geodetic techniques*. Journal of Geodesy, 85: 887-907. https://doi.org/10.1007/s00190-011-0508-5

HORVATH I., ESSEX E.A. 2003. *The southern-hemisphere mid-latitude day-time and night-time trough at low-sunspot numbers*. Journal of Atmospheric and Solar-Terrestrial Physics, 65: 917-940. https://doi.org/10.1016/S1364-6826(03)00113-5

ISHIDA T., OGAWA Y., KADOKURA A., HIRAKI Y., HÄGGSTRÖM I. 2014. *Seasonal variation and solar activity dependence of the quiet-time ionospheric trough*. Journal of Geophysical Research: Space Physics, 119: 6774-6783. https://doi.org/10.1002/2014JA019996

JAKOWSKI N., MAYER C., HOQUE M.M., WILKEN V. 2011. *Total electron content models and their use in ionosphere monitoring*. Radio Science, 46: 2010RS004620. https://doi.org/10.1029/2010RS004620

KOMJATHY A., SPARKS L., WILSON B.D., MANNUCCI A.J. 2005. *Automated daily processing of more than 1000 ground-based GPS receivers for studying intense ionospheric storms*. Radio Science, 40: 2005RS003279. https://doi.org/10.1029/2005RS003279

KRANKOWSKI A., SHAGIMURATOV I.I., EPHISHOV I.I., KRYPIAK-GREGORCZYK A., YAKIMOVA G. 2009. *The occurrence of the mid-latitude ionospheric trough in GPS-TEC measurements*. Advences in Space Research, 43: 1721-1731. https://doi.org/10.1016/j.asr.2008.05.014

KRYPIAK-GREGORCZYK, A., WIELGOSZ, P., 2018. *Carrier phase bias estimation of geometry-free linear combination of GNSS signals for ionospheric TEC modeling*. GPS Solutions, 22: 45. https://doi.org/10.1007/s10291-018-0711-4

KULLEN A., BRITTNACHER M., CUMNOCK J.A., BLOMBERG L.G. 2002. *Solar wind dependence of the occurrence and motion of polar auroral arcs: A statistical study*. Journal of Geophysical Research: Space Physics, 107. https://doi.org/10.1029/2002JA009245

LEE I.T., WANG W., LIU J.Y., CHEN C.Y., LIN C.H. 2011. *The ionospheric midlatitude trough observed by FORMOSAT-3/COSMIC during solar minimum*. Journal of Geophysical Research: Space Physics, 116. https://doi.org/10.1029/2010JA015544

LI Z., YUAN Y., WANG N., HERNANDEZ-PAJARES M., HUO X. 2015. *SHPTS: towards a new method for generating precise global ionospheric TEC map based on spherical harmonic and generalized trigonometric series functions*. Journal of Geodesy, 89: 331-345. https://doi.org/10.1007/s00190-014-0778-9

LUBYK K., HOQUE M.M., STOLLE C. 2022. *Evaluation of the Mid-Latitude Ionospheric trough Using GRACE Data*. Remote Sensing, 14: 4384. https://doi.org/10.3390/rs14174384

NILSSON H., SERGIENKO T.I., EBIHARA Y., YAMAUCHI M. 2005. *Quiet-time mid-latitude trough: influence of convection, field-aligned currents and proton precipitation*. Annales Geophysicae, 23: 3277-3288. https://doi.org/10.5194/angeo-23-3277-2005

NING Y., TANG J. 2018. *Study of ionospheric disturbances over the China mid- and low-latitude region with GPS observations*. Annales Geophysicae, 36: 81-89. https://doi.org/10.5194/angeo-36-81-2018

ORÚS R., HERNÁNDEZ-PAJARES M., JUAN J.M., SANZ J. 2005. *Improvement of global ionospheric VTEC maps by using kriging interpolation technique*. Journal of Atmospheric and Solar-Terraetrial Physics, 67: 1598-1609. https://doi.org/10.1016/j.jastp.2005.07.017

PAZIEWSKI J. 2015. *Precise GNSS single epoch positioning with multiple receiver configuration for medium-length baselines: methodology and performance analysis*. Measurement Science of Technology, 26: 035002. https://doi.org/10.1088/0957-0233/26/3/035002

PEREVALOVA N.P., ROMANOVA E.B., TASHCHILIN A.V. 2020. *Detection of high-latitude ionospheric structures using GNSS*. Journal of Atmospheric and Solar-Terrestrial Physics, 207: 105335. https://doi.org/10.1016/j.jastp.2020.105335

PRIKRYL, P., JAYACHANDRAN P.T., CHADWICK R., KELLY T.D. 2015. *Climatology of GPS phase scintillation at northern high latitudes for the period from 2008 to 2013*. Annales Geophysicae, 33: 531-545. https://doi.org/10.5194/angeo-33-531-2015

PRYSE S.E., KERSLEY L., MALAN D., BISHOP G.J. 2006. *Parameterization of the main ionospheric trough in the European sector*. Radio Science, 41: 2005RS003364. https://doi.org/10.1029/2005RS003364

REN X., ZHANG X., XIE W., ZHANG K., YUAN Y., LI X. 2016. *Global Ionospheric Modelling using Multi-GNSS: BeiDou, Galileo, GLONASS and GPS*. Scientific Reports, 6: 33499. https://doi.org/10.1038/srep33499

RODGER A. 2008. *The Mid-Latitude Trough-Revisited*. In: P.M. Kintner, A.J. Coster, T. Fuller-Rowell, A.J. Mannucci, M. Mendillo, R. Heelis (Eds.), Geophysical Monograph Series. American Geophysical Union, Washington, D. C., 25-33. https://doi.org/10.1029/181GM04

ROYERSMITH B., KNIPP D., STARR G., MORTON Y.J., MRAK S. WU, Q., 2025. *Robust Global Analysis of Mid-Latitude Ionospheric Trough Morphology*. Journal of Geophysical Research: Space Physics, 130: e2024JA033605. https://doi.org/10.1029/2024JA033605

SIERADZKI R. 2015. *An analysis of selected aspects of irregularities oval monitoring using GNSS observations*. Journal of Atmospheric and Solar-Terrestial Physics, 129: 87-98. https://doi.org/10.1016/j.jastp.2015.04.017

SIERADZKI R., PAZIEWSKI J. 2019. *GNSS-based analysis of high latitude ionospheric response on a sequence of geomagnetic storms performed with ROTI and a new relative STEC indicator*. Journal of Space Weather and Space Climate, 9: A5. https://doi.org/10.1051/swsc/2019001

TSAGOURI I., BELEHAKI A. 2015. *Ionospheric forecasts for the European region for space weather applications*. Journal of Space Weather and Space Climate, 5: A9. https://doi.org/10.1051/swsc/2015010

TSURUTANI B.T., ECHER E., SHIBATA K., VERKHOGLYADOVA O.P., MANNUCCI A.J., GONZALEZ W.D., KOZYRA J.U., PÄTZOLD M. 2014. *The interplanetary causes of geomagnetic activity during the 7–17 March 2012 interval: a CAWSES II overview*. Journal of Space Weather and Space Climate, 4: A02. https://doi.org/10.1051/swsc/2013056

WAUTELET G., WARNANT R. 2014. *Climatological study of ionospheric irregularities over the European mid-latitude sector with GPS*. Journal of Geodesy, 88: 223-240. https://doi.org/10.1007/s00190-013-0678-4

WERNER S., PRÖLSS G.W. 1997. *The position of the ionospheric trough as a function of local time and magnetic activity*. Advences in Space Research, 20: 1717-1722. https://doi.org/10.1016/S0273-1177(97)00578-4